

Electronic Structure Distortions in Chromium Chelates Impair Redox Kinetics in Flow Batteries

Jonathan R. Thurston, Keith P. White, Max Kudisch, Luis Kitsu Iglesias, Julia Lorenzetti, Francesco Bernasconi, Michael F. Toney, Michael P. Marshak, and David Reber*

Aminopolycarboxylate chelates are emerging as a promising class of electrolyte materials for aqueous redox flow batteries, offering tunable redox potentials, solubility, and pH stability through careful selection of ligands and transition metal ions. Despite their potential, the impact of molecular structure modifications on the electronic and electrochemical properties of these chelates remains underexplored. Here, we examine how introducing a hydroxyl group, often employed for its solubilizing properties, to the backbone of CrPDTA, a reference chelate material, significantly changes the thermodynamics and kinetics of the chelate's redox process. We correlate changes in molecular and electronic

structures to different electrochemical responses resulting from the hydroxyl addition and show that the introduction of this functional group leads to a distortion in the octahedral coordination of chromium. Furthermore, increased anisotropic spin density and nonintegral oxidation state changes in the Cr metal center result in a larger barrier for electron transfer in CrPDTA-OH. It is demonstrated that preserving a hexacoordinate chelate structure across a broad pH range is crucial for efficient flow battery application and it is emphasized that ligand modifications must avoid distorting the octahedral coordination of the transition metal.

1. Introduction

The chelation of transition metals with organic ligands can completely change the pH stability, redox potentials, kinetics, and solubility of compounds that are of importance to batteries, homogeneous catalysis, wastewater treatment, and biochemistry.^[1,2] Aminopolycarboxylates (APC) are a class of polydentate ligands that have emerged as components of highly reducing aqueous redox flow battery (RFB) negative electrolyte materials due to their ability to increase stability over a wide pH range through strong multicoordinate binding motifs. Iron or

chromium, for example, can be chelated to improve the solubility and pH stability of these cost-effective raw materials, enabling 2 V-class aqueous RFB chemistries.^[3–7] Single-crystal X-ray data shows that chromium forms a highly reducing pentacoordinate chelate with ethylenediaminetetraacetate (EDTA),^[8,9] leaving one carboxylate arm unbound in solution and allowing water to coordinate.^[10] However, this pentacoordinate structure renders the material unsuitable as a negative electrolyte, as the coordination of water to chromium in its reduced state is hypothesized to catalyze the hydrogen evolution reaction (HER).^[3] Adding a methylene group to the diamine backbone allows for the ligand,

J. R. Thurston
Department of Chemistry
University of Colorado – Boulder
Boulder, CO 80309, USA

K. P. White, M. F. Toney
Materials Science and Engineering Program
University of Colorado – Boulder
Boulder, CO 80309, USA

M. Kudisch
Chemistry & Nanoscience Department
National Renewable Energy Laboratory
Golden, CO 80401, USA

L. K. Iglesias, M. F. Toney
Department of Chemical and Biological Engineering
University of Colorado – Boulder
Boulder, CO 80309, USA

J. Lorenzetti, F. Bernasconi, D. Reber
Empa Swiss Federal Laboratories for Materials Science and Technology
8600 Dübendorf, Switzerland
E-mail: david.reber@empa.ch

J. Lorenzetti
École Polytechnique Fédérale de Lausanne
Institut des Matériaux
1015 Lausanne, Switzerland

F. Bernasconi
ETH Zürich
Department of Materials
8093 Zürich, Switzerland

M. F. Toney
Renewable and Sustainable Energy Institute
University of Colorado – Boulder
Boulder, CO 80309, USA

M. P. Marshak
Department of Chemistry
University of Wyoming
Laramie, WY 82072, USA

 Supporting information for this article is available on the WWW under <https://doi.org/10.1002/batt.202500250>

 © 2025 The Author(s). *Batteries & Supercaps* published by Wiley-VCH GmbH. This is an open access article under the terms of the Creative Commons Attribution License, which permits use, distribution and reproduction in any medium, provided the original work is properly cited.

1,3-diaminopropane-*N,N,N',N'*-tetraacetate (PDTA), to wrap around the metal center more effectively, reducing strain in the equatorial plane enough for the fourth carboxylate arm to coordinate to the metal center.^[3,11,12] The resulting CrPDTA chelate is stable in both its reduced and its oxidized states and emerges as one of the most competitive negative electrolyte materials for near-neutral pH aqueous RFBs.^[13] The excellent stability of CrPDTA in RFB cycling is linked to the hexacoordinate structure remaining also in solution, which excludes water from the inner coordination shell, preventing participation of the chelate in catalyzing water reduction. Understanding the impact of ligand modifications on the active material is thus crucial to designing better metal chelate RFB electrolytes. Over the past decade, many organic molecules have been considered for aqueous organic RFBs leading to identification of design trends; the addition of hydrophilic moieties to viologens, quinones and other organic frameworks, for example, was shown to drastically increase solubilities.^[14,15] Functional groups like -OH, -NH₂, -SO₃H, and -PO₃H₂ are particularly well suited to improve organic molecule aqueous solubility due to their hydrogen bonding ability, acidity, and polarity.^[16–18] In conjugated organic molecules, the addition of such groups is, however, associated with a shift in the molecule's reduction potential.^[19,20] Substituting aromatic rings with electron-donating groups such as -OH or -NH₂ decreases the electron affinity of the molecule and shifts the redox potential to more negative values, while electron-withdrawing group substitutions (-COOH, -PO₃H₂, -CF₃, -NO₂) show an opposite effect.^[16,19,21] Structural modifications thus require careful consideration to strike a balance between solubility and reduction potential, as these metrics directly affect the batteries' energy and power densities.

Therefore, extending these strategies to metal-organic chelates offers a promising approach to improving neutral pH RFBs. Here, we synthesize and characterize a chromium chelate, CrPDTA-OH, introducing a hydroxyl substituent with inductive electron-withdrawing properties to the central carbon atom of the alkyl backbone of PDTA.^[22] We study the impact of this modification on reduction potential and reaction kinetics, alongside a detailed analysis of the chelate's molecular and electronic structure, complementing X-ray photoelectron spectroscopy (XPS) with electron paramagnetic resonance spectroscopy (EPR). Our findings reveal that the introduction of the OH group induces significant changes in electrochemical behavior, which are driven by alterations in the Cr metal center's electronic properties stemming from differences in bonding with chelating atoms, that is, distortions of the octahedral coordination sphere. We then conduct RFB cycling experiments and directly link battery Coulombic inefficiencies to parasitic water reduction through *in situ* gas chromatographic hydrogen analysis. Our results show how metal-ligand binding motifs may suppress the HER and provide guidance for developing new chelating ligands for application in RFBs.

2. Results and Discussion

2.1. Synthesis and Electrochemical Characterization

KCrPDTA-OH was synthesized based on literature methods^[3,23] and purified via recrystallization, yielding dark red crystals.

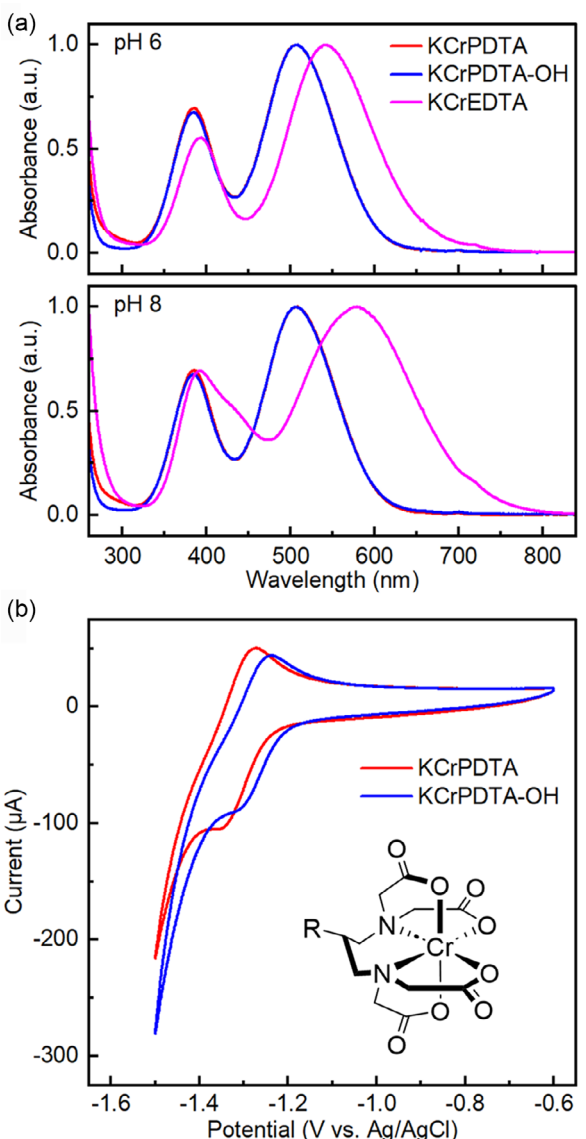


Figure 1. Characterization of chelates. a) UV-V is absorption spectra of aqueous KCrPDTA, KCrPDTA-OH, and KCrEDTA solutions at pH 6 and 8, normalized to the $^4A_{2g} \rightarrow ^4T_{2g}$ transition. b) Cyclic voltammograms of 5 mM KCrPDTA and KCrPDTA-OH in 1 M KCl, 0.1 M borate buffer (pH 9) using bismuth-plated glassy carbon electrodes with a scan rate of 100 mV s⁻¹. The Lewis structure of the chelates is shown in the inset, R = H in CrPDTA and R = OH in CrPDTA-OH.

KCrPDTA-OH exhibits a UV-V is spectrum characteristic of hexacoordinate chromium chelates (Figure 1a).^[24] After verifying the reported molar absorptivity of the $^4A_{2g} \rightarrow ^4T_{2g}$ transition of 116 M⁻¹ cm⁻¹ at 506 nm using a known concentration of KCrPDTA-OH, the maximum solubility of KCrPDTA-OH was determined as 0.70 M, compared to the previously determined solubility of 1.3 M for KCrPDTA.^[24,25] This decrease in solubility contradicts conventional assumptions in which the addition of hydrophilic groups to organic molecules enhances aqueous solubility, highlighting the fact that metal-organic chelates cannot be treated the same.

For comparison, CrEDTA, where a water molecule displaces one ligand arm, exhibits absorption peaks at much lower energies, as evident from its purple color.^[24] The water molecule in

this pentacoordinate complex is deprotonated in alkaline environments ($pK_a = 7.39$), drastically changing the properties of the, now blue, chelate.^[10] In contrast, CrPDTA and CrPDTA-OH show no differences in their absorption spectra between pH 6 and 8, suggesting that their hexacoordinate structure remains intact, which is assumed to be critical for RFB integration (Figure 1a).^[3] These binding motifs do not allow direct comparison of CrEDTA and CrPDTA/CrPDTA-OH in the pH range of interest, and to understand the effect of hydroxyl substitution on chelate properties we focus on the latter in the following discussion.

The effect of substitution on chelate electrochemical response was examined using cyclic voltammetry (CV).^[3,26] The redox reaction was not observable for KCrPDTA-OH using a standard glassy carbon electrode, as water reduction occurred before reducing the active material (Figure S1, Supporting Information). The electrode was thus plated with bismuth, an electrocatalyst known to reduce the charge transfer resistance.^[27–29] The redox reactions of both KCrPDTA and KCrPDTA-OH can be clearly observed on the modified electrode with reduction potentials of -1.31 and -1.27 V versus Ag/AgCl, respectively (Figure 1b). Previous studies on aromatic organic molecules show that the addition of electron-withdrawing groups shifts the reduction potential to more positive values, for example, the addition of a sulfonic acid group ($-\text{SO}_3\text{H}$) to hydroquinone increased the redox potential by ≈ 150 mV.^[20,30,31] The shift observed for CrPDTA-OH can potentially be explained by the inductive electron-withdrawing effect exhibited by the hydroxyl group and is investigated below. CV measurements recorded at different scan rates provide diffusion coefficients of 2.51×10^{-5} and $1.63 \times 10^{-5} \text{ cm}^2 \text{ s}^{-1}$, and reduction rate constants of 6.67×10^{-9} and $1.36 \times 10^{-11} \text{ cm s}^{-1}$, for CrPDTA and CrPDTA-OH, respectively (Figure S2, Supporting Information). CrPDTA-OH has a slightly lower diffusion coefficient, which can be explained by the molecule's larger size and an increase in hydrogen bonding interactions between the hydroxyl group and surrounding water

molecules. These factors contribute to a larger solvated radius, which is evidenced by higher viscosity and lower ionic conductivity (Table S1 and S2, Supporting Information). More interestingly, CrPDTA-OH exhibits a reduction rate constant two orders of magnitude lower than that of CrPDTA suggesting inefficient electron transfer because of changes in the chelate's electronic structure. Note that these measurements are for qualitative comparison of the two chelates only, as the surface area of the plated electrodes is not known.

2.2. Chelate Structural Characterization

To understand the stark differences in electrochemical activity, single-crystal X-ray diffraction (XRD) was used to compare the structures of KCrPDTA to KCrPDTA-OH. The molecular structure obtained from XRD of the hydroxylated derivative is shown in Figure 2a, exhibiting a hexacoordinate, pseudo-octahedral structure analogous to CrPDTA (Figure S3, Supporting Information) in which the two amino groups and four carboxylate arms are bound to the Cr metal center. The equatorial ligand atoms are defined in the horizontal plane and consist of N1, N2, O2, and O6, while the axial ligand atoms consist of O4 and O8. The bond lengths in CrPDTA-OH do not vary significantly from those of CrPDTA. The deviation of the equatorial oxygens bond angle (O2–Cr–O6) from 90° is used as a measure of strain for APC chelates.^[32] CrPDTA-OH exhibits a larger equatorial oxygen angle than CrPDTA, 100.5° versus 99.4° , respectively, indicating a more distorted octahedron. Additionally, the bond angle between the axial oxygens (O2–Cr–O8) deviates further from 180° , 173.2° for CrPDTA-OH versus 176.2° for CrPDTA. The larger deviations in both angles for CrPDTA-OH indicate that the carboxylate arms cannot wrap around the Cr center to bond as effectively, that is, with less orbital overlap, to achieve an octahedral geometry. Additional bond lengths and angles are given in Table S3, Supporting Information, and refinement details are shown in Table S4, Supporting Information.

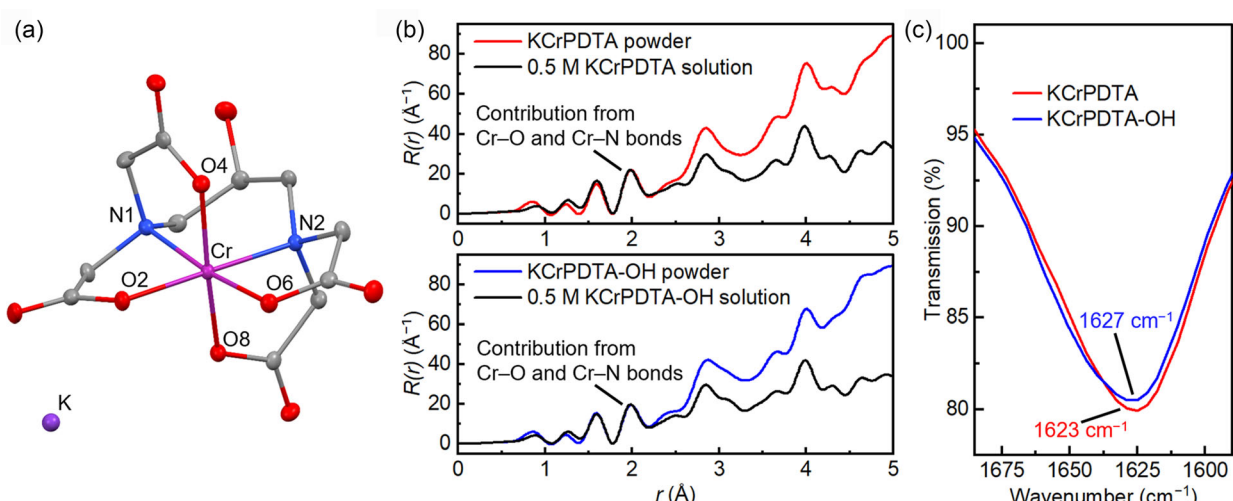


Figure 2. Chelate structural characterization. a) Crystal structure of KCrPDTA-OH showing 50% probability ellipsoids, Cr atom in magenta, K atom in purple, O atoms in red, N atoms in blue, C atoms in gray. The Cr metal center, K cation, and coordinating atoms are labeled. One water of hydration and hydrogen atoms are omitted for clarity. b) Weighted radial distribution function, $R(r)$, spectra of the powder and 0.5 M solution (pure water spectra subtracted) for KCrPDTA and KCrPDTA-OH. c) FTIR spectra of 0.5 M KCrPDTA and KCrPDTA-OH with the water background subtracted in the range of the COO^- bands.

The chelate structures in solution were studied via X-ray total scattering and Fourier-transform infrared spectroscopy (FTIR). X-ray total scattering provides structural information from the scattering of interatomic pairs through pair distribution function (PDF) analysis, providing information on the short- and long-range structure of materials. This allows for the comparison of solid state and solution structure.^[33,34] The $G(r)$ spectra (where r is the interatomic distance), derived from the Fourier transform of the corrected and normalized X-ray total scattering data, show distances between neighboring atoms. The $R(r)$ spectra represent the weighted radial distribution function which allows direct quantification of coordination numbers by integrating the area under the peak.^[35] For both materials, PDF were measured of the solid material and of 0.5 M solutions to evaluate the coordination of chromium in solid and in solution. The $G(r)$ spectra (Figure S4, Supporting Information) show peaks at $\approx 1.95 \text{ \AA}$ associated with the Cr—O and Cr—N bonds in the chromium coordination sphere for both chelates. To verify the chromium coordination, the PDF of the solids was fit using the XRD atomic parameters as the initial configuration and constraining the fit with the symmetry exhibited in the crystal structure, orthorhombic and monoclinic, respectively, for KCrPDTA and KCrPDTA-OH. Full fitting details are described in the Supporting Information (Methods and Table S5 and S6, Supporting Information). As expected, and corroborating the XRD structure, the chromium is hexacoordinate in the solid state for both materials (Figure S5, Supporting Information). The $R(r)$ spectra (Figure 2b) were then used to compare coordination numbers in the solid and solution (water-subtracted) phases. By integrating the area of the peak associated with the Cr—O and Cr—N bonds at $\approx 1.95 \text{ \AA}$, coordination numbers of 6 were obtained for both KCrPDTA and KCrPDTA-OH in solution, in agreement with our UV-V is analysis. We conclude that coordination of chromium in both chelates remains hexacoordinate in solution, an important consideration for RFB negative electrolytes to prevent water splitting.^[3,10,36]

To further investigate the chromium bonding environment, FTIR spectra of 0.5 M chelate solutions were recorded. Metal-APC chelation involves covalent bonding through electron sharing between the electron-dense carboxylate and electron-deficient metal center.^[37,38] For FTIR, it has been shown that chelation of the carboxylate to the metal center results in a larger electron localization on the carbonyl group by disturbing carboxylate resonance, resulting in more single bond character to the group and a redshift of the ligand carbonyl band to lower frequencies with stronger chelation.^[37] In the FTIR spectra of KCrPDTA and KCrPDTA-OH (Figure 2c and S6, Supporting Information), one carbonyl band is present at $\approx 1625 \text{ cm}^{-1}$ for each chelate, indicating that the four carboxylate arms remain chelated in solution.^[26,38] A blueshift of $\approx 4 \text{ cm}^{-1}$ to higher frequencies is observed for the carbonyl band of CrPDTA-OH indicating weaker chelation compared to that of CrPDTA. This implies that the octahedral distortion observed in the XRD structure persists in solution and suggests that the slower redox kinetics observed in electrochemical tests are related to less efficient Cr—O orbital overlap resulting from increased octahedral distortion, hindering electron transfer.

2.3. Chromium Electronic Structure Characterization

Our data indicates that the observed variations in electrochemical response stem from alterations in the chromium electronic structure due to modifications of the chelate geometry. To better understand how the hydroxyl addition affects the Cr metal center electronic structure, we used XPS and EPR to investigate the disparities in the electrochemical response.

Traditionally, XPS has been applied to probe the surface chemistry of more extensive molecular structures while studies of the intricate interactions within smaller molecular compounds are less common.^[39–41] XPS spectra of transition metals, oxides, and hydroxides are well recorded in the literature and the Cr 2p spectra is most commonly used for the chromium core level analysis due to its sensitivity to changes in oxidation state and large photoionization cross section at the Al K α X-ray energy.^[42–45] In the photoemission process, the outer valence configuration of the emitting element (i.e., Cr) screens photoelectron core-hole interactions of photoejected electrons, reducing the measured kinetic energy of these electrons. The strength of these screening interactions governs the measured binding energy position of core level electrons.^[46] As such, XPS of the Cr 2p core electrons provides a proxy for the electron density surrounding chromium.

Chromium is notable in that it exhibits complex multiplet splitting behavior in XPS spectra. This splitting arises from the interaction between unpaired d-electrons of the Cr(III) ion and the core hole formed during the photoemission process. The resulting multiple, nearly degenerate, final states lead to a characteristic distribution of peaks in the spectral envelope, reflecting both spin-orbit coupling and exchange interactions. Shifts in the magnitude of multiplet peak intensities and positions can thus be indicative of changes in the effective electron density (i.e., oxidation state) on the emissive element due to different coordinating ligand environments.^[44] XPS data was recorded for both compounds, including a wide spectrum showing no elemental impurities (Figure S7, Supporting Information) and high-resolution spectra of the Cr 2p, C 1s and K 2p, N 1s, and O 1s core levels. In the Cr 2p spectra (Figure 3a and S8, Supporting Information), it is evident that the Cr 2p_{1/2} and 2p_{3/2} peaks for CrPDTA-OH are shifted to higher binding energies by $\approx 0.4 \text{ eV}$ compared to CrPDTA, indicating a more electron-deficient Cr metal center in CrPDTA-OH. For context, a shift in binding energy of 0.4 eV corresponds to the difference observed between Cr(III) peaks in Cr(OH)₃ and Cr₂O₃.^[44] This shift results from less covalent character in the chelate bonds, supporting our hypothesis of reduced electron sharing from the ligand atoms to the Cr metal center shown in the FTIR data, and explains the positively shifted redox potential of CrPDTA-OH compared to CrPDTA. For full fitting details and ligand XPS spectra/analyses, see Supporting Information Methods, and Figure S9–S11.

To understand the differences in redox kinetics we complement our XPS analysis with EPR measurements. EPR is used to provide additional electronic structure information on paramagnetic systems such as Cr(III) ($d^3, S = 3/2$) by probing the local environment and interactions of unpaired electrons. EPR was performed on frozen aqueous solutions for each chelate. Spectra were simulated to elucidate the magnitude of the axial

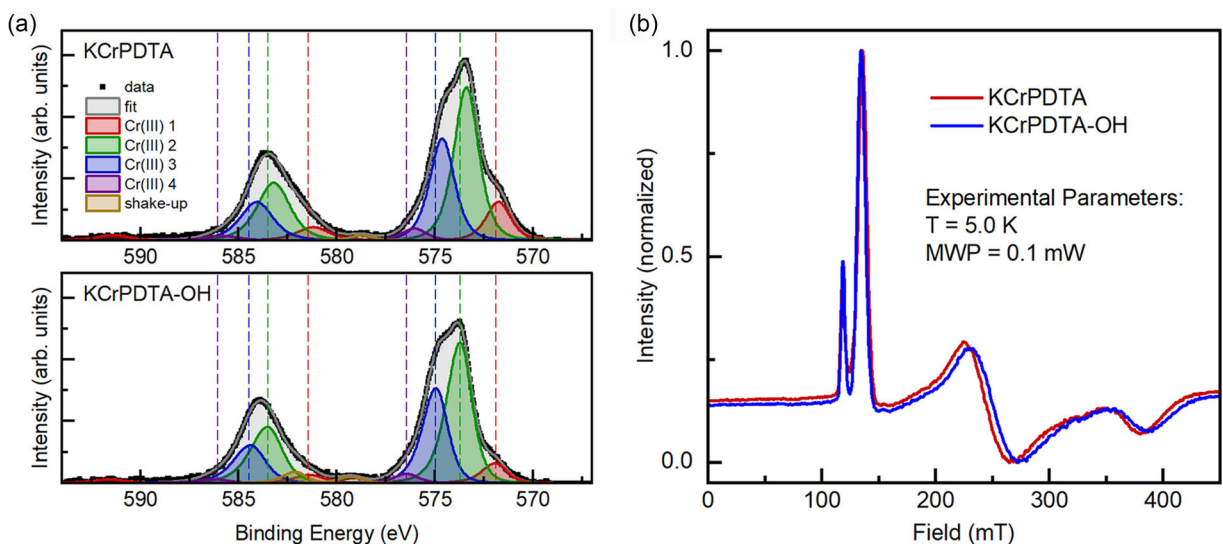


Figure 3. Electronic structure characterization. a) Fitted Cr 2p XPS spectra for KCrPDTA and KCrPDTA-OH powder samples, with dashed lines in both spectra indicating the binding energy of KCrPDTA-OH component peak centers. b) Experimental X-band EPR spectra for frozen aqueous solutions of KCrPDTA and KCrPDTA-OH.

zero-field-splitting parameter, $|D|$, and the associated rhombicity, $\lambda = E/D$ (where E is the rhombic zero-field-splitting parameter), which is a measure of the asymmetry in the electron density distribution around a paramagnetic center. Simulated spectra were computed using a model incorporating a distribution of λ values as has been previously done in a study on Cr(III) chelates for catalysis.^[47] In $S = 3/2$ systems where $|D|$ is larger than the microwave frequency used for EPR measurements, the spectral line shape and effective g -values are determined predominately by λ which is very sensitive to small changes in the coordination environment.^[48]

The EPR spectra (Figure 3b) contain two sharp features for both KCrPDTA and KCrPDTA-OH at comparable field magnitudes of 118 and 135 mT that are assigned via simulation as the $M_s = \pm 3/2$ (B parallel to z -axis) and $M_s = \pm 1/2$ (B parallel to y -axis) transitions, respectively. Two additional $M_s = \pm 1/2$ transitions are observed, the first at ≈ 200 – 350 mT (B parallel to x -axis) and the second at ≈ 400 – 450 mT (B parallel to z -axis) and extending beyond the experimental window. Both transitions occur at higher fields for KCrPDTA-OH compared to KCrPDTA, consistent with increased rhombicity in KCrPDTA-OH. As such, the spectra agree well with simulations computed using models (Figure S12 and Supporting Information Methods) containing identical parameters except for an increased rhombicity (KCrPDTA, $\lambda = 0.200$; KCrPDTA-OH $\lambda = 0.212$) and a larger full width half maximum (FWHM, proportional to λ). The increased rhombicity in KCrPDTA-OH indicates a directional asymmetry in electron density, consistent with the XRD and FTIR data showing decreased molecular symmetry, compared to KCrPDTA. It was previously reported that an increase in rhombicity in $S = 1/2$ Cu(II) active sites of proteins correlates with an increase in the activation barrier for electron transfer, retarding the redox kinetics.^[49] A similar correlation between rhombicity and redox kinetics is observed herein, where KCrPDTA-OH exhibits higher rhombicity and slower redox kinetics relative to KCrPDTA. Thus, the

increase in rhombicity may be associated with an increased barrier for electron transfer, potentially arising from the structural distortions away from ideal octahedral geometry described above.

Furthermore, the larger FWHM for KCrPDTA-OH suggests increased fluctuation in the solution-state coordination geometry, consistent with the hydrogen bonding capability in aqueous solution introduced by the presence of the hydroxyl group. In $S = 5/2$ Fe(III) complexes, an increase in rhombicity was observed with decreasing temperature that was ascribed to perturbations of hydrogen bonding interactions in solid state, supporting our interpretation that supramolecular interactions influence the rhombicity of the chelate.^[50] As such, the EPR data is consistent with the viscosity and ionic conductivity data which indicates that increased hydrogen bonding contributes to the slower diffusion observed upon reduction/oxidation for KCrPDTA-OH.

2.4. Battery Integration

To corroborate our spectroscopic investigation under practical conditions, the three chelates studied here were used as negative electrolytes in full-cell RFBs using ligands as buffers (Figure 4a,b and S13a, Supporting Information).^[29] The ferro/ferricyanide redox couple, a common positive electrolyte,^[3,20,51,52] was used in excess to ensure all variations between the cells resulted from the capacity limiting chromium negative electrolytes. The cells were cycled at 100 mA cm^{-2} with lower and upper voltage cutoffs of 0.7 and 2 V, respectively. CrPDTA-OH exhibits a significantly lower average Coulombic efficiency of 98.2% compared to 99.3% for CrPDTA. The addition of the hydroxyl group and larger solvated radius, as evidenced by decreased diffusivity, may transport more water to the electrode surface upon polarization, making water more readily available to be reduced at the electrode in a static system. However, given the forced convection in the flow cell setup, mass transport limitation of water is unlikely to

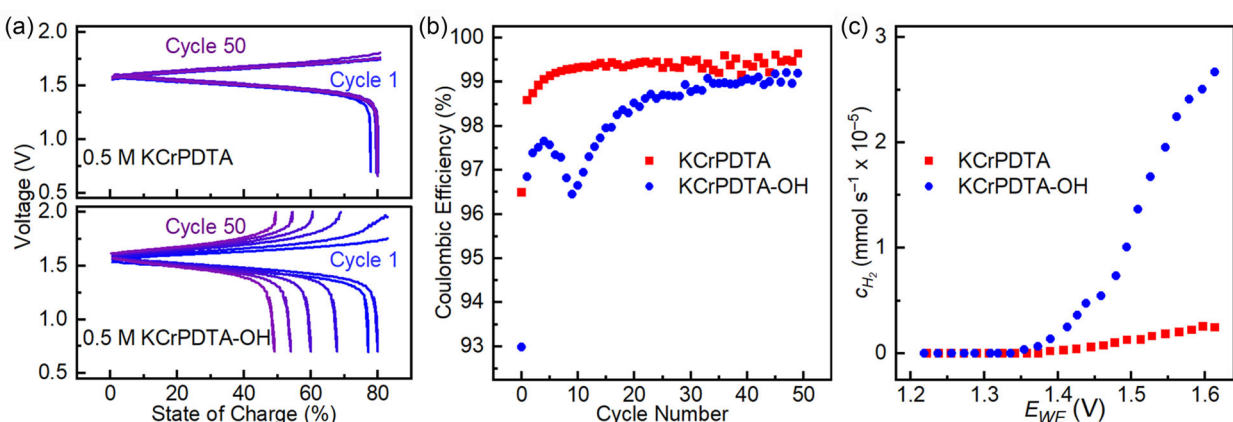


Figure 4. Comparison in RFBs. a) Voltage profiles of RFBs containing 0.5 M KCrPDTA or KCrPDTA-OH negative electrolyte, respectively, cycled at 100 mA cm⁻², and b) The corresponding Coulombic efficiencies. c) Hydrogen generation during linear voltage sweeps in full cells.

dominate hydrogen evolution rates, and we hypothesize that the slower redox kinetics of the active material result in more electrons being available for side reactions, such as HER, per unit time. This hypothesis was tested by performing linear sweep voltammetry on fresh cells while sampling the headspace of the negative electrolyte reservoir via gas chromatography for hydrogen. This allows precise determination of the HER onset potential as well as the cell voltage-dependent hydrogen generation rate. Voltage sweeps were performed at 0.05 mV s⁻¹ from 1.2 to 1.7 V, and the gas was sampled in five-minute intervals (Figure 4c). The onset of hydrogen generation is detected at 1.35 and 1.38 V with CrPDTA-OH and CrPDTA, respectively. While similar overall currents are observed (Figure S13b, Supporting Information), the hydrogen generation rate is an order of magnitude higher with CrPDTA-OH, consistent with its lower Coulombic efficiency in RFB tests. The comparable hydrogen generation onset potentials but markedly different hydrogen generation rates suggest that fewer electrons are taken up by CrPDTA-OH per unit time compared to CrPDTA. This provides a clear demonstration of the slower redox kinetics of CrPDTA-OH, caused by structural distortions, leading to decreased Coulombic efficiency in high-voltage RFBs.

The CrPDTA-OH cell also exhibits pronounced capacity fading (Figure 4a and S13a, Supporting Information). pH-dependent CV and UV-V is experiments reveal that both CrPDTA and CrPDTA-OH lose their redox activity above pH 12, likely due to hydroxide ions gradually displacing the ligand arms (Figure S14, Supporting Information). This chemical degradation is accompanied by a color change from red to blue around pH 12, resembling the behavior of pentacoordinate CrEDTA near pH 8 (Figure 1a), and the eventual formation of green precipitates above pH 13, consistent with the formation of Cr(OH)₃. The UV-V is spectrum of CrPDTA-OH after battery cycling corroborates pH-induced degradation, showing a shift to longer wavelengths characteristic of pentacoordinate ligand binding while the spectrum of the CrPDTA electrolyte remains unchanged (Figure 1a and S13c, Supporting Information). Notably, even though the hydrogen generation rate is much higher with CrPDTA-OH, the bulk pH of the CrPDTA-OH electrolyte after battery cycling was lower (increased from 9.6 to 9.8) than for CrPDTA (increased from 9.5

to 9.9), suggesting that hydroxyl groups derived from water reduction are consumed in the CrPDTA-OH solution, most likely by binding to chromium as suggested by our spectroscopic analysis. The rapid rise in local pH driven by water reduction thus causes capacity fading as hydroxides displace the ligand arms.

These challenges are even more pronounced with CrEDTA electrolytes. With this pentacoordinate chelate that has a hydroxyl bound to chromium at pH 9.5, we observe an average Coulombic efficiency of only 96.9% and much faster capacity fading as homogeneous water reduction is catalyzed by the chromium center already with the first charge cycle (Figure S15, Supporting Information). This interpretation is supported by a significantly lower hydrogen generation onset potential of 1.28 V and pronounced water reduction. The hydrogen generation is so extensive even at relatively low cell voltages that the current and hydrogen flow rate peak at 1.5 V, likely due to electrode surface area being blocked by gas bubbles (Figure S15d,e, Supporting Information). This highlights the critical importance of maintaining hexacoordinate chelation that excludes water from the coordination sphere and a more regular chelation geometry for efficient electron transfer as key design principles for developing metal-organic chelates as negative electrolytes in aqueous RFBs.

3. Conclusion

We explored the impact of APC ligand modifications on the molecular and electronic structure, as well as the electrochemical behavior, of KCrPDTA and its hydroxyl-modified derivative KCrPDTA-OH. Crystallographic and X-ray total scattering analyses revealed that KCrPDTA-OH exhibits a more distorted pseudo-octahedral geometry compared to KCrPDTA, which persists in solution. FTIR, XPS, and EPR analyses further showed that the hydroxyl group introduces electron deficiency at the chromium metal center, raising the redox potential and hindering electron transfer through weaker ligand-metal orbital overlap. These structural distortions result in sluggish redox kinetics and an increased propensity for hydrogen evolution during flow battery

operation. Our findings highlight the critical role of maintaining a hexacoordinate structure and minimizing octahedral distortions to optimize ligand–metal interactions for high-performance RFB negative electrolytes, as a distorted coordination geometry results in decreased metal–ligand orbital overlap, which in turn leads to slower redox kinetics and more pronounced water reduction, causing pH-induced material degradation. Future studies should explore the role of electron-donating or -withdrawing substituents and longer carboxylate arms to disentangle the effects of octahedral distortion and electronic modifications on redox behavior and stability.^[53–61]

Additional Information

The authors have cited additional references within the Supporting Information

Deposition Number(s) <https://www.ccdc.cam.ac.uk/services/structures? id = doi:https://doi.org/10.1002/batt.202500250 2391652> (for KCrPDTA), 2391651 (for KCrPDTA-OH) contain(s) the supplementary crystallographic data for this paper. These data are provided free of charge by the joint Cambridge Crystallographic Data Centre and Fachinformationszentrum Karlsruhe <http://www.ccdc.cam.ac.uk/structures> Access Structures service.

Acknowledgements

The pair distribution function research used beamline 28-ID-1 of the National Synchrotron Light Source II, a US Department of Energy (DOE) Office of Science User Facility operated for the DOE Office of Science by Brookhaven National Laboratory under Contract No. DE-SC0012704. The authors thank Keenan Wyatt for his assistance in collecting the data. The X-ray photoelectron spectroscopy data was collected at the COSINC facility at CU Boulder. Electron paramagnetic resonance measurements and analysis were performed at NREL using the Advanced Spin Resonance Facility with funding provided by the US Department of Energy, Office of Science, as part of BioLEC EFRC under grant no. DE-SC0019370. This work was funded in part by the National Science Foundation under grant no. 2155227. J.R.T. was funded in part by the King Fellowship for this work. D.R. acknowledges funding from the Swiss National Science Foundation (SNSF) Ambizione Fellowship Z00P2_209078. D.R. also thanks Corsin Battaglia and Empa's Laboratory Materials for Energy Conversion for hosting his research group. This work was authored in part by the National Renewable Energy Laboratory, operated by Alliance for Sustainable Energy, LLC, for the U.S. Department of Energy (DOE) under contract no. DE-AC36-08GO28308. The views expressed in the article do not necessarily represent the views of the DOE or the U.S. Government. The U.S. Government retains and the publisher, by accepting the article for publication, acknowledges that the U.S. Government retains a nonexclusive, paid-up, irrevocable, worldwide license to publish or reproduce the published form of this work, or allow others to do so, for U.S. Government purposes.

Conflict of Interest

The authors declare no conflict of interest.

Data Availability Statement

The data that support the findings of this study are available from the corresponding author upon reasonable request.

Keywords: chelates · electronic structures · flow batteries · molecular structures · redox kinetics

- [1] R. A. Marcus, *J. Chem. Phys.* **1956**, *24*, 966.
- [2] Y.-W. D. Chen, K. S. V. Santhanam, A. J. Bard, *J. Electrochem. Soc.* **1981**, *128*, 1460.
- [3] B. H. Robb, J. M. Farrell, M. P. Marshak, *Joule* **2019**, *3*, 2503.
- [4] A. S. N. Murthy, T. Srivastava, *J. Power Sources* **1989**, *27*, 119.
- [5] D. Xi, A. M. Alfaraidi, J. Gao, T. Cochard, L. C. I. Faria, Z. Yang, T. Y. George, T. Wang, R. G. Gordon, R. Y. Liu, M. J. Aziz, *Nat. Energy* **2024**, *9*, 479.
- [6] S. E. Waters, C. M. Davis, J. R. Thurston, M. P. Marshak, *J. Am. Chem. Soc.* **2022**, *144*, 17753.
- [7] P. Schröder, D. Obendorf, T. Bechtold, *ChemElectroChem* **2019**, *6*, 3311.
- [8] R. N. F. Thorneley, A. G. Sykes, *Chem. Commun.* **1968**, *340*.
- [9] L. E. Gerdom, N. A. Baenziger, H. M. Goff, *Inorg. Chem.* **1981**, *20*, 1606.
- [10] K. Kanamori, K. Kawai, *Inorg. Chem.* **1986**, *25*, 3711.
- [11] R. Herak, G. Srdanov, M. I. Djuran, D. J. Radanović, M. Bruvo, *Inorg. Chim. Acta* **1984**, *83*, 55.
- [12] J. A. Weyh, R. E. Hamm, *Inorg. Chem.* **1968**, *7*, 2431.
- [13] S. E. Waters, B. H. Robb, S. J. Scappaticci, J. D. Saraidaridis, M. P. Marshak, *Inorg. Chem.* **2022**, *61*, 8752.
- [14] T. Liu, X. Wei, Z. Nie, V. Sprenkle, W. Wang, *Adv. Energy Mater.* **2016**, *6*, 1501449.
- [15] K. Wedege, E. Dražević, D. Konya, A. Bentien, *Sci. Rep.* **2016**, *6*, 39101.
- [16] S. Jin, Y. Jing, D. G. Kwabi, Y. Ji, L. Tong, D. De Porcellinis, M.-A. Goulet, D. A. Pollack, R. G. Gordon, M. J. Aziz, *ACS Energy Lett.* **2019**, *4*, 1342.
- [17] Y. Ji, M.-A. Goulet, D. A. Pollack, D. G. Kwabi, S. Jin, D. De Porcellinis, E. F. Kerr, R. G. Gordon, M. J. Aziz, *Adv. Energy Mater.* **2019**, *9*, 1900039.
- [18] M.-A. Goulet, M. J. Aziz, *J. Electrochem. Soc.* **2018**, *165*, A1466.
- [19] J. R. Thurston, S. E. Waters, B. H. Robb, M. P. Marshak, in *Encyclopedia of Energy Storage* (Ed: L. F. Cabeza), Elsevier, Oxford **2022**, pp. 423–435.
- [20] K. Lin, Q. Chen, M. R. Gerhardt, L. Tong, S. B. Kim, L. Eisenach, A. W. Valle, D. Hardee, R. G. Gordon, M. J. Aziz, M. P. Marshak, *Science* **2015**, *349*, 1529.
- [21] K. Lin, R. Gómez-Bombarelli, E. S. Beh, L. Tong, Q. Chen, A. Valle, A. Aspuru-Guzik, M. J. Aziz, R. G. Gordon, *Nat. Energy* **2016**, *1*, 16102.
- [22] J. C. Robles, Y. Matsuzaka, S. Inomata, M. Shimoji, W. Mori, H. Ogino, *Inorg. Chem.* **1993**, *32*, 13.
- [23] D. Pletcher, J. C. P. White, *Electrochim. Acta* **1992**, *37*, 575.
- [24] M. Hecht, F. A. Schultz, B. Speiser, *Inorg. Chem.* **1996**, *35*, 5555.
- [25] S. E. Waters, J. R. Thurston, R. W. Armstrong, B. H. Robb, M. P. Marshak, D. Reber, *J. Power Sources* **2022**, *520*, 230877.
- [26] D. Reber, J. R. Thurston, M. Becker, G. F. Pach, M. E. Wagoner, B. H. Robb, S. E. Waters, M. P. Marshak, *Appl. Mater. Today* **2022**, *28*, 101512.
- [27] A. D. Proctor, B. H. Robb, J. D. Saraidaridis, M. P. Marshak, *J. Electrochem. Soc.* **2022**, *169*, 030506.
- [28] J. Xu, Y. Zhang, Z. Huang, C. Jia, S. Wang, *Energy Fuels* **2021**, *35*, 8617.
- [29] T. Echeverria, F. Bernasconi, P. P. Ziemiański, D. Reber, *Batter. Supercaps* **2025**, *8*, e202400696.
- [30] B. Yang, L. Hooyer-Burkhardt, F. Wang, G. K. S. Prakash, S. R. Narayanan, *J. Electrochem. Soc.* **2014**, *161*, A1371.
- [31] B. Yang, L. Hooyer-Burkhardt, S. Krishnamoorthy, A. Murali, G. K. S. Prakash, S. R. Narayanan, *J. Electrochem. Soc.* **2016**, *163*, A1442.
- [32] T. Yamamoto, K. Mikata, K. Miyoshi, H. Yoneda, *Inorg. Chim. Acta* **1988**, *150*, 237.
- [33] D. A. Keen, *J. Appl. Cryst.* **2001**, *34*, 172.
- [34] P. Juhás, T. Davis, C. L. Farrow, S. J. L. Billinge, *J. Appl. Cryst.* **2013**, *46*, 560.
- [35] P. F. Peterson, D. Olds, M. T. McDonnell, K. Page, *J. Appl. Cryst.* **2021**, *54*, 317.
- [36] H. Ogino, T. Nagata, K. Ogino, *Inorg. Chem.* **1989**, *28*, 3656.
- [37] D. H. Busch, J. C. Jr. Bailar, *J. Am. Chem. Soc.* **1953**, *75*, 4574.

- [38] D. T. Sawyer, J. M. McKinnie, *J. Am. Chem. Soc.* **1960**, *82*, 4191.
- [39] D.-B. Wang, B.-H. Chen, B. Zhang, Y.-X. Ma, *Polyhedron* **1997**, *16*, 2625.
- [40] D. P. Drolet, D. M. Manuta, A. J. Lees, A. D. Katnani, G. J. Coyle, *Inorg. Chim. Acta* **1988**, *146*, 173.
- [41] A. Cano, L. Reguera, M. Avila, D. Velasco-Arias, E. Reguera, *Eur. J. Inorg. Chem.* **2020**, *2020*, 137.
- [42] M. C. Biesinger, B. P. Payne, A. P. Grosvenor, L. W. M. Lau, A. R. Gerson, R. S. C. Smart, *Appl. Surf. Sci.* **2011**, *257*, 2717.
- [43] B. W. Veal, A. P. Paulikas, *Phys. Rev. B* **1985**, *31*, 5399.
- [44] M. C. Biesinger, C. Brown, J. R. Mycroft, R. D. Davidson, N. S. McIntyre, *Surf. Interface Anal.* **2004**, *36*, 1550.
- [45] I. Grohmann, E. Kemnitz, A. Lippitz, W. E. S. Unger, *Surf. Interface Anal.* **1995**, *23*, 887.
- [46] F. de Groot, A. Kotani, *Core Level Spectroscopy of Solids*, CRC Press, Boca Raton, FL **2008**.
- [47] N. A. Hirscher, C. H. Arnett, P. H. Oyala, T. Agapie, *Organometallics* **2020**, *39*, 4420.
- [48] S. Ye, *Magn. Reson. Lett.* **2023**, *3*, 43.
- [49] J. K. Ma, F. S. Mathews, V. L. Davidson, *Biochemistry* **2007**, *46*, 8561.
- [50] A. Solano-Peralta, J. P. Saucedo-Vázquez, R. Escudero, H. Höpfl, H. El-Mkami, G. M. Smith, M. E. Sosa-Torres, *Dalton Trans.* **2009**, 1668, <http://dx.doi.org/10.1039/B814225D>.
- [51] E. M. Fell, D. D. Porcellinis, Y. Jing, V. Gutierrez-Venegas, T. Y. George, R. G. Gordon, S. Granados-Focil, M. J. Aziz, *J. Electrochem. Soc.* **2023**, *170*, 070525.
- [52] D. Reber, J. R. Thurston, M. Becker, M. P. Marshak, *Cell. Rep. Phys. Sci.* **2023**, *4*, 101215.
- [53] O. V. Dolomanov, L. J. Bourhis, R. J. Gildea, J. A. K. Howard, H. Puschmann, *J. Appl. Crystallogr.* **2009**, *42*, 339.
- [54] K. Momma, F. Izumi, *J. Appl. Crystallogr.* **2011**, *44*, 1272.
- [55] A. J. Bard, L. R. Faulkner, *Electrochemical Methods: Fundamentals and Applications*, 2nd ed., Wiley, New York, NY **2000**.
- [56] T.-M. Usher, D. Olds, J. Liu, K. Page, *Acta Crystallogr., Sect. A: Found. Adv.* **2018**, *74*, 322.
- [57] M. C. Biesinger, *Appl. Surf. Sci.* **2022**, *597*, 153681.
- [58] R. P. Gupta, S. K. Sen, *Phys. Rev. B* **1974**, *10*, 71.
- [59] R. P. Gupta, S. K. Sen, *Phys. Rev. B* **1975**, *12*, 15.
- [60] S. Stoll, A. Schweiger, *J. Magn. Reson.* **2006**, *178*, 42.
- [61] B. H. Robb, S. E. Waters, M. P. Marshak, *Dalton Trans.* **2020**, *49*, 16047.

Manuscript received: April 1, 2025

Revised manuscript received: April 9, 2025

Version of record online:
